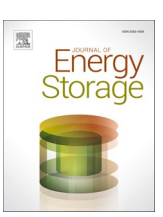
ELSEVIER

Contents lists available at ScienceDirect

Journal of Energy Storage

journal homepage: www.elsevier.com/locate/est



Research Papers

Experimental study on flow and heat transfer of a novel molten-salt-heat-exchanger for flue gas energy storage

Hongliang Su ^{a,b,d}, Jinliang Xu ^{a,b,c}, Xiongjiang Yu ^{a,b,c,*}, Xinyu Dong ^{b,e}, Chao Liu ^b, Yan Wang ^b, Jian Xie ^{a,b,c}, Qinghua Wang ^b, Yuguang Niu ^b, Jizhen Liu ^b, Ying Huang ^d, Anyou Dong ^b

- a Beijing Key Laboratory of Multiphase Flow and Heat Transfer for Low Grade Energy Utilization, North China Electric Power University, Beijing 100026, China
- ^b Beijing Huairou Laboratory, Beijing 101400, China
- c Key Laboratory of Power Station Energy Transfer Conversion and System, North China Electric Power University, Ministry of Education, Beijing 102206, China
- ^d Harbin Boiler Company Limited, Harbin 150046, China
- e Hebei Key Laboratory of Energy Storage and Integrated Energy Systems, North China Electric Power University, Baoding 071003, Hebei, China

ARTICLE INFO

Keywords: Flue gas Molten-salt-heat-exchanger Experiments Heat transfer Pressure drop

ABSTRACT

Developing flexible energy sources to support the grid's consumption of low-carbon energy is an effective means of addressing sustainable development and climate change. A flue gas-heated molten salt thermal storage technology has been proposed to decouple thermal systems and enhance operational flexibility of coal-fired power plants. To validate the core equipment, or the flue gas-molten salt heat exchanger, a 300 kW flue gas-molten salt thermal storage platform was established with molten salt temperature range of (290–569)°C, and flue gas temperature range of (327–657)°C. An experimental study of the flow and heat transfer of this heat exchanger indicates: (a) Existing correlations for the flue gas resistance show errors exceeding 27 % due to the novel inclined structure of both fins and tubes. A revised correlation based on experimental data is proposed with errors less than 20 %. (b) The heat absorption proportion of the lower module shows a positive linear relationship with the flue gas flow rate. Conversely, this proportion follows a negative exponential correlation with the molten salt flow rate. (c) The thermal deviation in the exchanger is negatively correlated with the molten salt flow rate while positively correlated with the flue gas temperature, peaking at 7.5 °C. This study systematically developed strategies for storing thermal energy from flue gas of coal-fired power plants into molten salt via experiments. The performance of the functional prototype was validated, thereby laying the foundation for its industrial application.

1. Introduction

The development of low-carbon energy systems is an important global measure to address sustainable development and climate change issues [1]. Many countries are actively adopting low-carbon or zero-carbon energy sources, such as wind and solar power, to replace and gradually phase out fossil fuels. However, these renewable energy sources inherently possess intermittent and stochastic characteristics that make them difficult to regulate [2]. As the proportion of unstable renewable energy in power grids continues to rise, it poses significant challenges to grid frequency [3], power quality, and power fluctuations [4]. To ensure grid stability and support the development of smart grids

[5], building flexible power sources [6,7] and large-scale energy storage facilities [8] is an emerging trend.

Among various forms of large-scale energy storage, thermal energy storage (TES) demonstrates notable advantages [9]. Molten salt-based TES, characterized by its high energy storage capacity, long storage duration, and low cost, has been widely applied in solar thermal power generation [10]. Molten salt is a compound formed by the combination of cations and anions [11]. Based on the types of anions, common molten salts can be classified into nitrate salts, chloride salts, fluoride salts, and carbonate salts. Fluoride salts exhibit excellent neutron characteristics, thermal performance, transport properties, and chemical stability, enabling the dissolution of fissile fuels as well as fission

E-mail address: yuxiongjiang@ncepu.edu.cn (X. Yu).



Received 18 March 2025; Received in revised form 30 June 2025; Accepted 2 August 2025 Available online 6 August 2025

^{*} Corresponding author at: Beijing Key Laboratory of Multiphase Flow and Heat Transfer for Low Grade Energy Utilization, North China Electric Power University, Beijing 100026, China.

products. They serve as key materials for Fluoride-salt-cooled Hightemperature Reactor (FHR) technology. However, due to the high cost of FLiBe and the chemical toxicity of beryllium, fluoride salts have not gained broader applications [12]. Carbonate salts are not directly used as heat transfer fluids, with research primarily concentrated on Molten Salt Oxides (MSO) and Molten Carbonate Fuel Cells (MCFC) [13]. While MCFC has achieved a global installed capacity exceeding 300 MW, issues such as rapid voltage decay and low energy conversion efficiency hinder competitive commercial viability [14]. MSO technology remains at the pilot or experimental scale, where carbonate salts are employed for processing organic waste like PVC, biomass, and resins [15]. Among various molten salts, nitrate salts (e.g., Solar Salt, Hitec, and Hitec XL) demonstrate the widest industrial applications. Solar Salt was first implemented in solar tower thermal power plants in 1984. By serving dual roles as both heat transfer and energy storage media in Concentrated Solar Power (CSP) systems, nitrate salts decouple heat absorption and power generation processes, directly addressing the randomness and uncontrollability of renewable energy sources, thereby establishing CSP as a grid-friendly renewable energy solution [16]. As of 2023, CSP constitutes 0.17 % of global renewable energy installed capacity [17]. Compared to the relatively mature nitrate salts, chloride salts possess superior thermal stability and lower costs, making them one of the most promising materials for next-generation thermal energy storage technologies. Ding et al. [18] reviewed the selection processes of chloride salts among major research groups, identifying the MgCl₂/KCl/NaCl mixture as the most promising. Lambrecht et al. [19] highlighted Mg-Na-K and Zn-Na-K chlorides for their low melting points and wide operational temperature ranges in CSP applications. Nearly all studies agree that the critical challenge for commercialization lies in addressing the corrosion issues of chloride salts on metallic materials [18,19].

In countries like China, coal-fired power remains a dominant energy source. Integrating TES into the thermal cycle of coal-fired power plants to enhance their operational flexibility presents promising prospects. While techniques such as extracting steam from coal-fired units to heat molten salts for energy storage have been extensively explored [20–22], they also reveal unresolved technical challenges. Compared to the steam extraction heat storage systems, results of flue gas thermal energy storage systems demonstrate superior performance and economic viability, achieving an equivalent round-trip efficiency of 83.5 % [23]. The flue gas-molten salt heat exchanger (FSHE), as a core component of flue gas heat storage, deserves special attention.

One significant application of FSHE is peak load regulation in coal-fired power plants. Flue gas serves as an upstream energy carrier throughout the energy transfer and conversion processes in thermal power stations. The "single-phase to single-phase" heat exchange between flue gas and molten salt fundamentally addresses the "narrow temperature difference" issue associated with steam extraction-based thermal storage, offering advantages such as high energy storage efficiency, economic viability, and safety. In coal-fired plants, when boilers are at low load, a certain flow rate of flue gas is directly extracted to heat low-temperature molten salt for storage. During grid load increasing, the high-temperature molten salt can reheat feedwater and generate additional steam to rapidly boost inlet flow of turbine and significantly enhance the plant's load-following capability. Additionally, flue gas

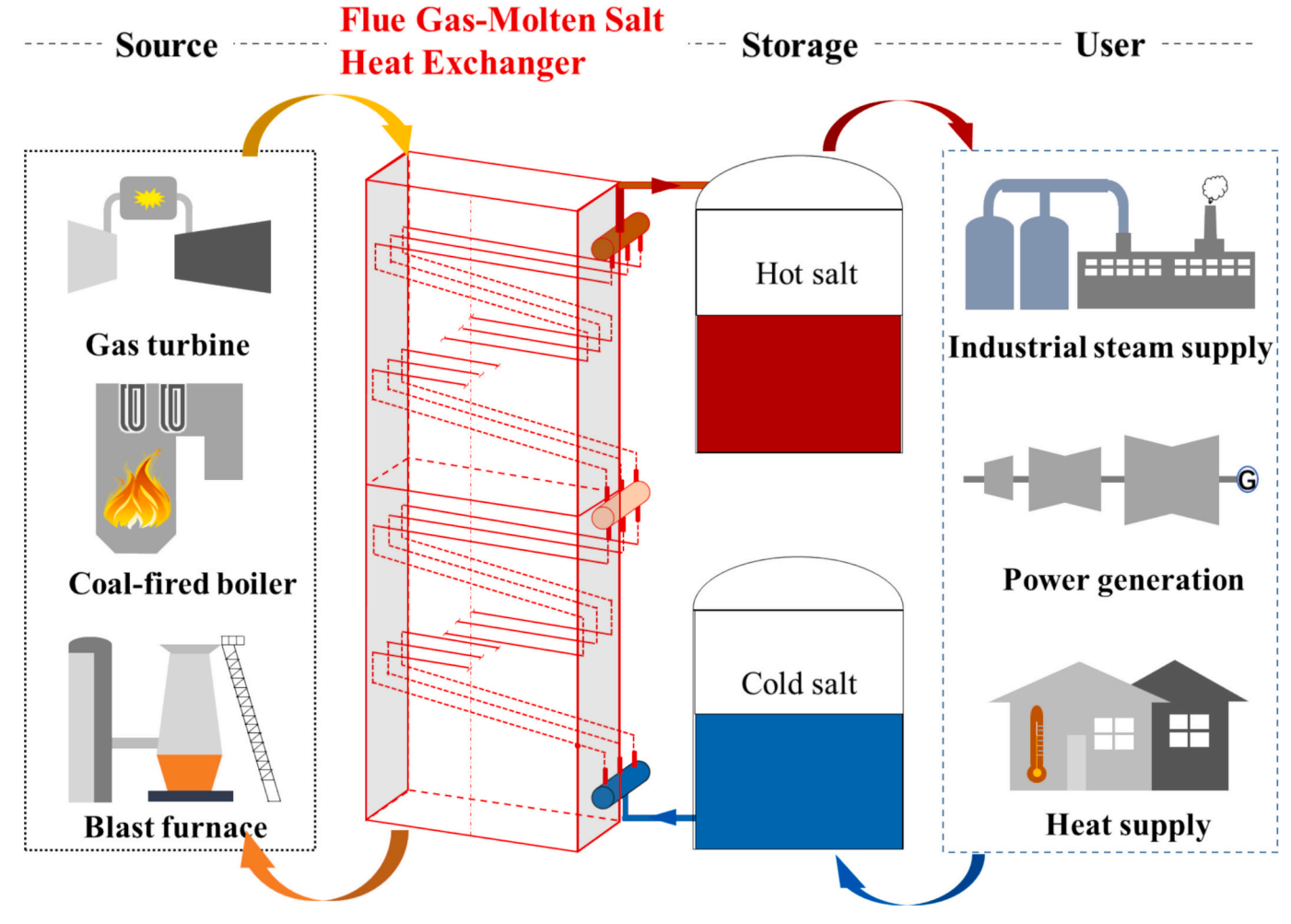


Fig. 1. Potential application of flue gas driven molten salt heat storage.

streams are prevalent in industries such as metallurgy and steel production [24]. These high-quality thermal energy sources, often underutilized due to their intermittent and dispersed nature, can be efficiently stored using flue gas-molten salt heat exchange technology for industrial steam supply and heating purposes as shown in Fig. 1, thereby reducing energy waste.

While the application of flue gas as a heat source for molten saltbased TES holds great promise, relevant research remains insufficient. Though extensive experimental studies exist on single-tube heat transfer of molten salt fluids [25-29], these investigations focus only on heat transfer characteristics instead of the final application design. The thermal design of heat exchangers is comprehensively influenced by factors including flow patterns, fluid phase transitions, structural configurations, and material properties, necessitating experimental research on full-scale FSHE. Research on molten salt-water/steam and molten salt-oil heat exchangers [30-38] has gained significant attention due to their applications in CSP, yet experimental studies on FSHE are scarce. Chen et al. [39,40] conducted experiments on serpentine-coil crossflow and staggered-tube heat exchangers, while Qian et al. [41] investigated finned-tube heat exchangers – all using air rather than coalfired flue gas as the external fluid. The complex composition and high fouling propensity of coal-fired flue gas, containing substantial particulate matter, render air-based experimental results inapplicable to practical scenarios. Although Mu et al. [42,43] and Jiang et al. [44] proposed novel FSHE configurations, their work primarily focused on developing dynamic nonlinear models and control strategies, with designs remaining conceptual. Guo et al. [45] briefly described a 300 kW prototype and simulated a 9.7 MW heat exchanger's steady/transient characteristics via Simulink, yet provided less experimental thermal performance data.

From concept to engineering application, this emerging technology still faces significant challenges in key equipment development, including: (1) mismatched heat resistance between gas and molten salt in heat exchangers, necessitating solutions to enhance external heat transfer, ash accumulation, and wear caused by dust in the flue gas; (2) to prevent tube blockage caused by salt solidification and salt decomposition due to high-temperature flue gas during exchanger shutdown, it is essential to address gravity-driven flow of molten salt after pump cessation; and (3) molten salts are prone to thermal decomposition under excessive temperatures. Overheating of individual tubes restricts the outlet temperature of the FSHE from reaching its design value, so thermal deviation control measures must be implemented in the heat exchanger design.

To address these challenges, we propose a flue gas-molten salt thermal storage process and its key equipment. Through pilot-scale experimental validation, this research not only confirms the engineering feasibility of the proposed design but also acquires critical experimental data that characterize the thermodynamic performance and flow resistance properties under actual operating conditions. These findings have successfully overcome the "last-mile" technical barriers between theoretical research and engineering applications, thereby laying a solid foundation for subsequent large-scale implementations. This paper is structured as follows: Section 2 elaborates on the proposed flue gasmolten salt thermal storage system, including its design and working principles. Section 3 details methodologies. Section 4 presents the experimental analysis results and discussion on the flow and heat transfer of the FSHE. The study specifically investigates the influence of flue gas and molten salt parameter variations on the thermal load distribution patterns in the heat exchanger under off-design conditions. Finally, Section 5 summarizes findings and outlines future research directions.

2. Experiments

2.1. Experimental system

As shown in Fig. 2, a flue gas-molten salt thermal storage platform was built by Beijing Huairou Laboratory and Harbin Boiler *Co.*, Ltd. The red loop represents a flue gas circuit, while the black and blue loops correspond to a molten salt circuit and a steam-water circuit, respectively.

The flue gas circuit serves as the heat source for the experimental system and consists of a 10 MW pulverized coal boiler and a thermal storage bypass. The thermal storage bypass includes a FSHE. In this setup, pulverized coal is combusted in the furnace to generate high-temperature flue gas. After being cooled by the convective heating surfaces, the flue gas is at an intermediate temperature range of 450–650 °C, which is suitable for experimental purposes. A damper allows free flow allocation of the flue gas between the boiler's flue duct and the thermal storage bypass. This configuration enables flexible regulation of the flue gas in the flue gas thermal storage bypass while ensuring that excess flue gas from the boiler is effectively cooled, preventing overheating and damage to downstream equipment.

To facilitate experimental studies on flow and heat transfer of flue gas and molten salt, the molten salt circuit was designed and constructed. Key components include two molten salt tanks, an outlet vessel, and the FSHE. Each molten salt tank has an effective volume of 9 $\rm m^3$, capable of accommodating approximately 18 tons of molten salt. During the thermal storage process, heat transfer between the flue gas and molten salt occurs through the FSHE. The flue gas enters from the top of the FSHE and flows over the outer surfaces of its heat transfer tubes. Simultaneously, low-temperature molten salt is pumped from the cold salt tank to the interior of the heat transfer tubes. After heat exchange, the heated molten salt flows back to the hot salt tank under gravitational force.

To efficiently release the stored thermal energy and facilitate continuous experimentation, the steam-water circuit was designed and implemented. This circuit includes a salt cooler, a water tank, and a plunger pump. The salt cooler adopts a kettle-type structure, with heat transfer tubes immersed in water. During the discharging process, high-temperature molten salt from the hot salt tank is pumped through the heat transfer tubes of the salt cooler, where it exchanges heat with saturated water outside the tubes. The maximum heat exchange power reaches 350 kW, which is comparable to the thermal storage power, enabling simultaneous charging and discharging processes. This capability ensures continuous operation during experimental testing.

As shown in Fig. 3, the flue gas-molten salt thermal energy storage platform is built on the 10 MW boiler belonging to Harbin Boiler Co., Ltd. The flue gas thermal storage bypass and a molten salt thermal storage unit are constructed for this platform. The boiler has a rated heat output of 10 MW, with a furnace cross-section of 2000 mm \times 2000 mm, a height of 27 m, a width of 3 m, and a length of 9 m, weighing a total of 140 tons. The boiler's designed coal consumption rate is 1.72 t/h, suitable for combusting anthracite, bituminous coal, and lignite.

The thermal storage bypass is connected in parallel with the original boiler flue, with its inlet directly accessing the rear turning chamber of the 10 MW boiler and its outlet redirecting the heat-exchanged flue gas back into the boiler for further cooling and utilization. The bypass consists of inlet and outlet sections equipped with adjustable dampers and an intermediate section housing the FSHE. The heat capacity of the FSHE is determined by the boiler. At a normal load of 5 MW , up to 70 % of the total flue gas extracted from the boiler is cooled from 650 °C to 450 °C, releasing a heat capacity around 300 kW. Thus, the capacity of the FSHE is determined as 300 kW to couple with the 10 MW boiler.

The molten salt storage unit is connected to the FSHE via three molten salt pipelines: one for inlet, one for outlet, and one overflow pipeline. To address potential molten salt freezing risks, all pipelines are inclined at a 3°-5° angle and equipped with Mineral Insulated (MI)

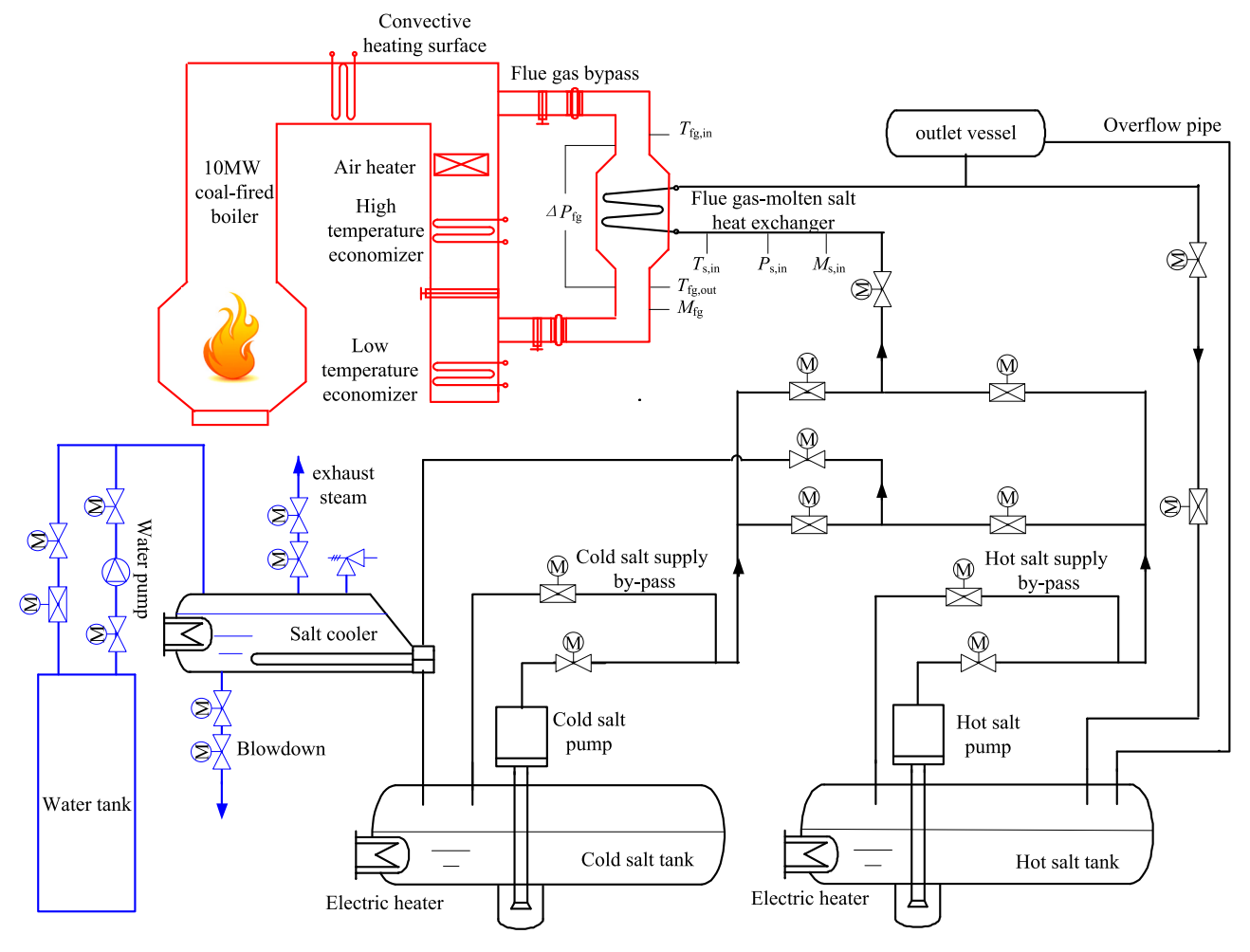


Fig. 2. Schematic diagram of the 300 kW flue gas-molten salt thermal storage platform.

electric heating devices. The construction of the molten salt storage unit includes two steel tiers, with the salt cooler installed on the upper tier for cooling high-temperature molten salt. Below are two cylindrical molten salt tanks, each 5 m long and 1.5 m in diameter, located at the lowest point of the molten salt circuit. This design ensures that all molten salt flows back into the tanks due to gravity during system shutdown, preventing freezing-induced safety hazards.

To characterize the heat transfer coefficients for the flue gas and molten salt, a single-variable experimental methodology was employed. Prior to experimentation, the cold salt tank was thermally conditioned to the target temperature through synergistic operation of the salt cooler and in-tank electric heating elements. During the experimental campaign, the flue gas temperature was modulated by adjusting boiler combustion intensity, whereas the flue gas flow rate was regulated via the thermal storage bypass and boiler flue dampers.

To maximize energy storage capacity with molten salts, the maximum working temperature in a molten salt thermal energy storage system is typically set close to the upper limit, while the minimum temperature is determined by the parameters of the heat-release medium. The binary nitrate used in this research platform features a maximum working temperature range of 260–560 °C·In terms of application scenarios, the most prevalent approach for molten salt energy storage in thermal power plants is to heat the boiler feedwater. Given that the feedwater temperature of boilers with subcritical parameters or higher exceeds 260 °C, the cold salt temperatures in the experimental protocol were designated as three sets, i.e.,290 °C, 320 °C, and 350 °C, after accounting for the heat transfer terminal difference.

Prior to each experiment, the molten salt in the cold salt tank was

preconditioned to match these three temperature sets. Thus, the FSHE inlet temperatures, which were also the cold salt temperatures, were first utilized for experimental protocols classification. In the variable flue gas flow experiments, the molten salt flow rate within the FSHE was maintained at a constant 1.7 $\rm m^3/h$. Each set of the FSHE inlet temperatures was further sub-classified according to three distinct flue gas temperature setpoints (450 °C, 550 °C, 650 °C) and three flue gas flow rate regimes (1500 $\rm Nm^3/h$, 2500 $\rm Nm^3/h$, 3500 $\rm Nm^3/h$). For experiments focusing on molten salt flow rate as the variable parameter, the flue gas flow rate was fixed at 3000 $\rm Nm^3/h$, with other experimental groupings following analogous protocols. Collectively, the experimental matrix encompassed over 50 operational runs, enabling comprehensive characterization of heat transfer dynamics.

2.2. The 300 kW FSHE

The 300 kW FSHE, a critical experimental apparatus in flue gas-molten salt thermal energy storage technology, is designed with upper and lower modular configurations. As shown in Fig. 4, each module measures 1400 mm in length, 380 mm in width, and 4955 mm in height. The two modules are connected via an intermediate header, which facilitates effective control of thermal deviation within the FSHE. In experimental operation, the flue gas and molten salt undergo countercurrent heat exchange: the flue gas enters from the top inlet of the FSHE and exits from the lower outlet, while the molten salt flows into the lower module at a lower elevation, passes through the intermediate header to enter the upper module, and finally exits from the upper module at a higher elevation.

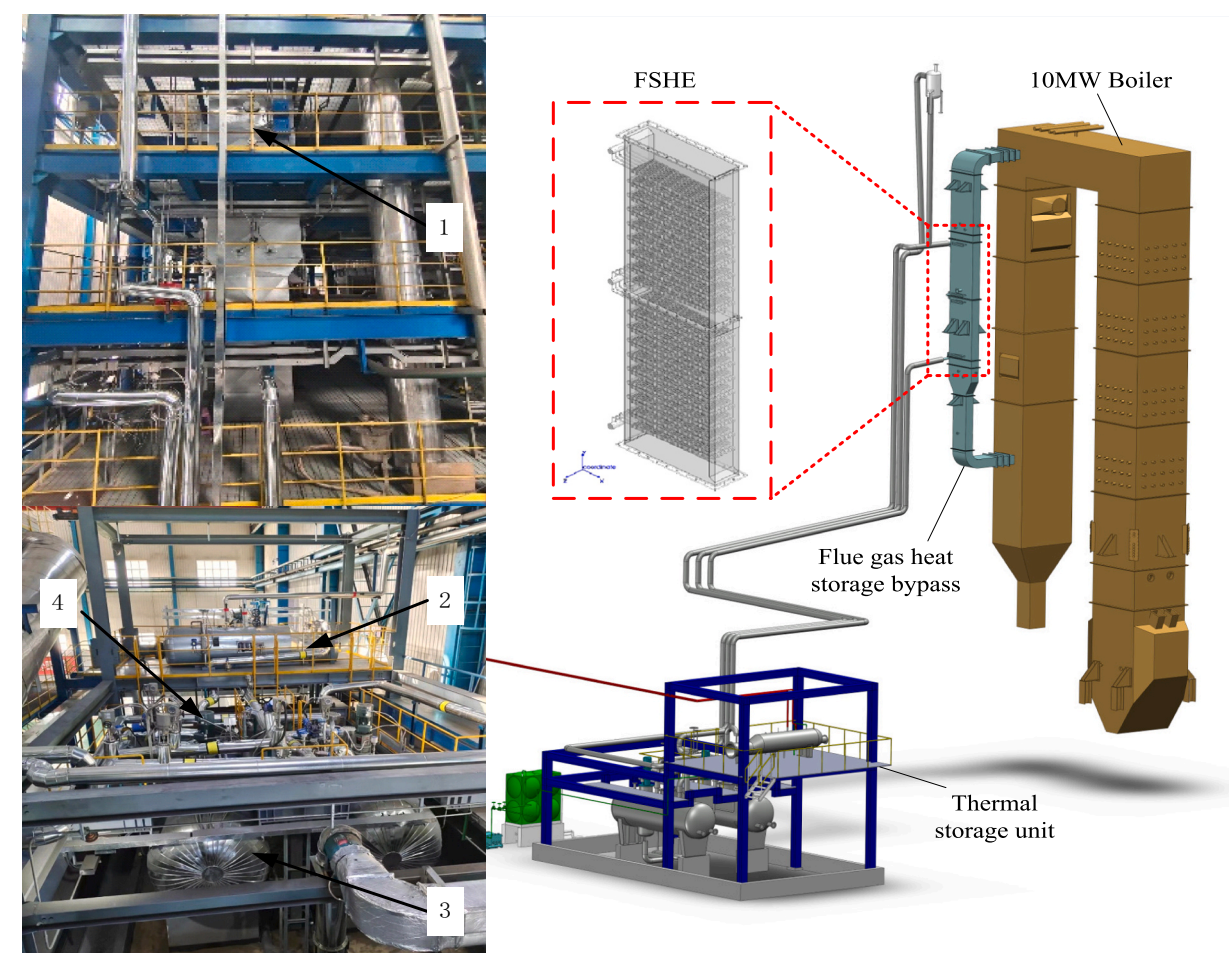


Fig. 3. The Arrangement of the 300 kW flue gas-molten salt thermal storage platform: 1 FSHE; 2 Salt cooler; 3 Salt tank; 4 Salt pump.

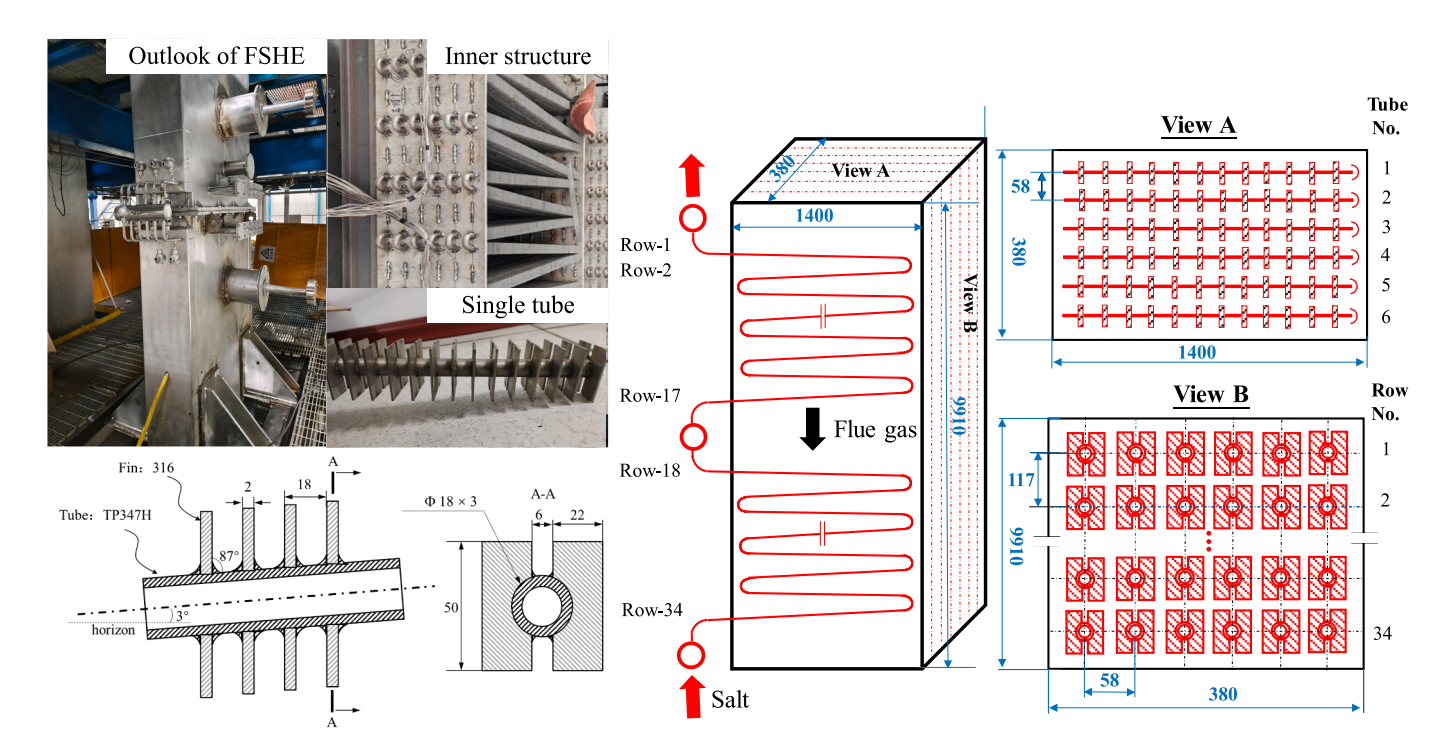


Fig. 4. The Structure of the FSHE.

Within each module, six heat transfer tubes are arranged in parallel, and along the flow direction of the flue gas, there are 34 rows of tubes spaced at 58 mm laterally and 117 mm longitudinally. To address the gravity-dependent salt drainage, the tubes are intentionally designed with an inclination. Drawing from established experimental apparatus configurations documented in Refs. [39,40], the tilt angle is specifically set at 3° relative to the horizontal axis. In the event of pump shutdown, the molten salt flows back to the storage tank by gravity without solidifying inside the tubes.

To enhance heat transfer performance, extended surfaces are incorporated on the heat transfer tubes. The base tubes have a specification of $\Phi 18 \times 3$ mm with a length of 1500 mm. On the outer surface of the tube bundle, single H-shaped fins are attached, each fin measuring 22 mm in height, 50 mm in width, and 2 mm in thickness. The spacing between adjacent fins is set to 18 mm. The tube exterior experiences conditions identical to conventional coal-fired boiler flue gas ducts, while the interior maintains similar with CSP molten salt loops. Thus, austenitic stainless steel TP347H is selected as the optimal tube material, leveraging its proven performance history in both coal-fired power plants and CSP. Although martensitic steels like T91 or T92 seem more cost-effective, the lack of systematic characterization regarding molten salt corrosion degradation mechanisms precludes immediate industrial deployment of these materials.

The FSHE is equipped with various instruments for measuring the temperature, the pressure, and the flow rates of the flue gas and molten salt: K-type sheathed thermocouples are used to measure the inlet and outlet temperatures of both flue gas and molten salt. The flow rates of the flue gas and molten salt are measured using two ultrasonic flowmeters (SICK FLOWSIC 100PH and OPTISONIC 4400HT). All measurement data are acquired using a Distributed Control System from Nanjing Sciyon Wisdom Technology Group Co., Ltd., with a sampling frequency of 1 Hz, ensuring accurate monitoring and analysis of the experimental conditions.

The FSHE utilizes a binary nitrate-based molten salt, whose composition is analyzed by SGS-CSTC Standards Technical Services (Tianjin) Co., Ltd. The mass fractions of sodium nitrate (NaNO₃) and potassium nitrate (KNO₃) were determined to be 59.5 % and 40.4 %, respectively, with trace impurities. The experimental boiler was fueled with Shenhua bituminous coal from China, characterized by a gross calorific value of 20.47 MJ/kg. The proximate analysis on an as-received basis was the following composition: carbon (C) 53.08 %, hydrogen (H) 3.22 %, oxygen (O) 9.18 %, nitrogen (N) 0.77 %, sulfur (S) 0.64 %, ash content 18.1 %, and moisture (M) 15 %. The flue gas originated from the downstream of the boiler flue, with adjustable temperature and flow rate. The maximum achievable temperature of flue gas was 700 °C, while the maximum flow rate of flue gas reached 3500 Nm³/h. The flue gas contained pollutants such as nitrogen oxides (NO_x) and sulfur oxides (SO_x), along with particulate matter. Typical flue gas composition included: 74.75 % N₂, 7.71 % CO₂, 0.07 % SO₂, 6.41 % H₂O, 11.09 % O₂, and a dust concentration of approximately 24 g/Nm³.

3. Data processing and analysis

3.1. Heat transfer capacity

The overall molten salt heat absorption of the FSHE can be written as

$$Q_{\rm s} = m_{\rm s} c_{\rm s,p} (T_{\rm s,out} - T_{\rm s,in}) \tag{1}$$

where $c_{s,p}$ represents the specific heat of the molten salt and is determined by the average temperature of molten salt at the FSHE inlet and outlet. m_s is the molten salt flow rate. $T_{s,in}$ and $T_{s,out}$ are the molten salt temperature at the FSHE inlet and outlet.

The FSHE is divided into two modules. Using the molten salt temperature $T_{\rm s,mid}$ in the intermediate header between the two modules, the heat exchange capacity of the lower module can be written as

$$Q_{\rm s1} = m_{\rm s}c_{\rm s.p}(T_{\rm s.mid} - T_{\rm s.in}) \tag{2}$$

The flue gas heat release capacity can be written as

$$Q_{fg} = m_{fg}c_{fg,p}(T_{fg,in} - T_{fg,out})$$

$$\tag{3}$$

In the formula, $c_{\rm fg,p}$ represents the specific heat of the flue gas and is determined by the flue gas composition, the inlet and outlet temperature of flue gas. $m_{\rm fg}$ is the flue gas flow rate. $T_{\rm fg,in}$ and $T_{\rm fg,out}$ are the flue gas temperature at the FSHE inlet and outlet.

3.2. Overall heat transfer coefficient

The logarithmic mean temperature difference (LMTD) of the FSHE can be written as

$$\Delta T_{\rm m} = \frac{\left(T_{\rm s,in} - T_{\rm fg,out}\right) - \left(T_{\rm s,out} - T_{\rm fg,in}\right)}{\ln\left(\frac{T_{\rm s,in} - T_{\rm fg,out}}{T_{\rm s,out} - T_{\rm fg,in}}\right)} \tag{4}$$

The overall heat transfer coefficient is the key data for the FSHE, which can be obtained by measuring the heat transfer rate and the LMTD of the exchanger, it can be written as

$$h_{\rm exp} = \frac{Q_{\rm s}}{A_{\rm o}\Delta T_{\rm m}} \tag{5}$$

The heat transfer process can also be expressed in terms of thermal resistance, where the overall thermal resistance can be represented as the sum of individual thermal resistances:

$$R = h_{\rm exp}^{-1} = R_{\rm i} + R_{\rm o} + R_{\rm w} + R_{\rm f} \tag{6}$$

In the formula, R_i is the thermal resistance on the molten salt side, R_o is the thermal resistance on flue gas side, $R_w = \frac{d_o}{2\lambda_w} \ln\left(\frac{d_o}{d_i}\right)$ is the thermal resistance of the metal tube wall, R_f is the fouling resistance on the outer tube surface. d_o is the outer tube diameter, d_i is the inner tube diameter, A_o is the heat transfer area based on the outer tube surface, λ_w is the thermal conductivity of the metal tube wall.

3.3. Heat transfer coefficient of the molten salt side

To obtain the molten salt heat transfer coefficient, soot blowing was performed before each experiment. During the experiments, the flue gas flow rate through the FSHE was maintained at approximately constant, while the molten salt flow rate was continuously varied. As shown in Eq. (6), when the conditions that the flue gas scouring on the outer tube surface and ash deposition remain unchanged (i.e., R_0 and R_f are stable), and the thermal resistance of the tube wall is negligible, the relationship between overall thermal resistance R and internal thermal resistance R_i should exhibit linearity.

By introducing the internal thermal resistance $R_i = \frac{1}{h_s} \frac{d_o}{d_i}$, Formula (6) can be rewritten as

$$h_{\rm exp}^{-1} = b_1 h_{\rm s}^{-1} + b_2 \tag{7}$$

In the formula, $b_1 = \frac{d_0}{d_i}$ and b_2 are constants, h_s is the molten salt heat transfer coefficient.

According to Wu's [28] heat transfer study of molten salt in circular tubes, the heat transfer coefficients for the transition and turbulent zone can be expressed by the following equations:

$$\begin{cases} Nu_{s,cal} = 0.00154Re_s^{1.1}Pr_s^{1/3}, Re_s < 10000 \\ Nu_{s,cal} = 0.0294Re_s^{0.787}Pr_s^{1/3}, Re_s > 10000 \end{cases}$$
(8)

Here, convective heat transfer coefficient of fully developed turbulence form in Eq. (8) is adopted, i.e., the form $h_s = b_0 \lambda_s R e_s^{0.8} P r_s^{0.33}$, Eq. (7) is rewritten as

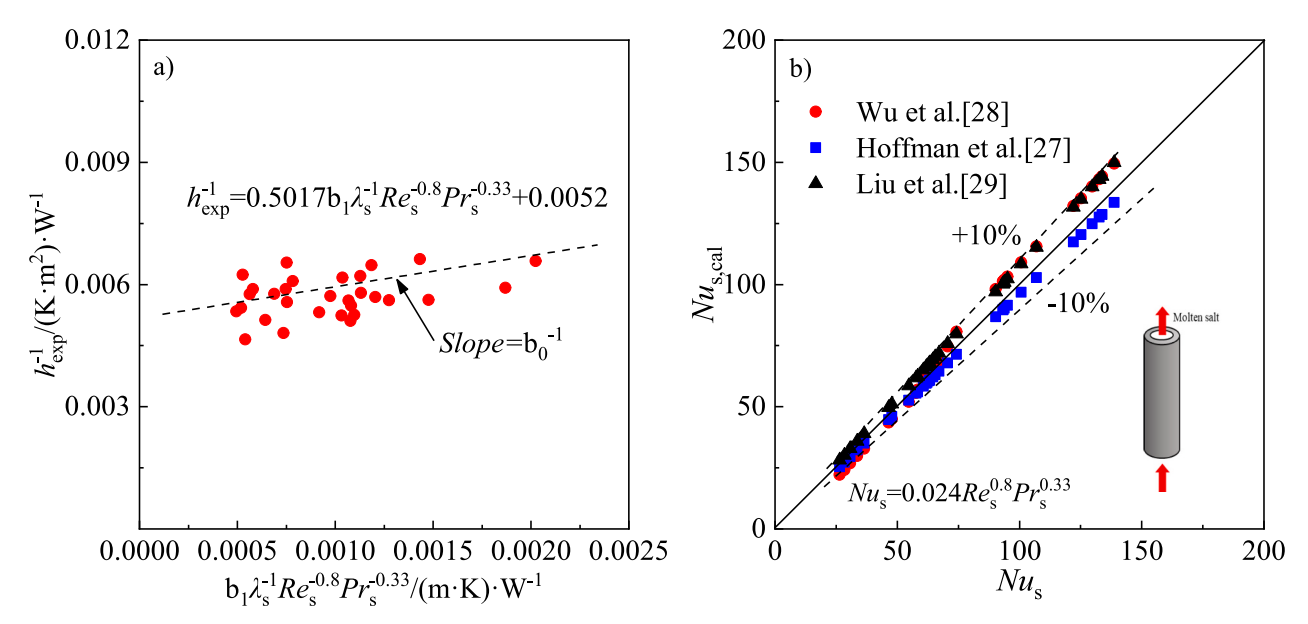


Fig. 5. The molten salt heat transfer coefficient of the FSHE: a) Linear relationship between $h_{\rm exp}^{-1}$ and $b_1 \lambda_{\rm s}^{-1} R e_{\rm s}^{-0.72}$, b) Comparison between the fitted curve and literature data.

$$h_{\rm exp}^{-1} = b_0^{-1} \left(b_1 \lambda_{\rm s}^{-1} Re_{\rm s}^{-0.8} Pr_{\rm s}^{-0.33} \right) + b_2 \tag{9}$$

where b_0 is a constant, Re_s is the Reynolds number of the molten salt, Pr_s is the Prandtl number of the molten salt, and λ_s is the thermal conductivity of the molten salt. The thermophysical properties of molten salt can be obtained from Ref. [46].

3.4. Heat transfer coefficient of the flue gas side

Similarly, the flue gas heat transfer coefficient can be determined using the same approach as that for the molten salt side. The molten salt flow rate in the FSHE is maintained at the rated flow rate, while the flue gas flow rate is varied in the experiment. As can be seen from Eq. (6), ignoring the thermal resistance of the tube wall, R and R_i are linear relationships.

Introducing $R_0 = \frac{1}{h_0}$, Eq. (6) can again be rewritten as

$$h_{\rm exp}^{-1} = h_{\rm fg}^{-1} + c_2 \tag{10}$$

where, c_2 is a constant, h_{fg} is the flue gas heat transfer coefficient.

Feng et al. [47] and Lin et al. [48] proposed correlations for the heat transfer coefficient $h_{\rm fg,t}$ of square finned tubes based on the total heated area (Eq. (11)). Based on the formulas and nomograms from Ref. [48], the applicable velocity range of these correlations is 4–15 m/s, the qualitative dimension range is 4–30 mm, and the flue gas temperature range is 100–700 °C. In the experiments of this study, the flue gas velocities are 4–9 m/s, the qualitative dimension of the heat exchanger is 18 mm, and the average flue gas temperatures are 400–550 °C. The velocities and temperatures of flue gas as well as characterized size of the tube are all within the application range of the correlations. Therefore, it is considered that the Reynolds number should also fall within this range, making Eq. (11) applicable to Eq. (10). The heat transfer coefficient $h_{\rm fg,cal}$ based on the outer surface of the tube can be obtained from Eq. (12).

$$h_{\rm fg,t} = 0.0957 \frac{\lambda_{\rm fg}}{S_{\rm p}} \left(\frac{d_{\rm o}}{S_{\rm p}}\right)^{-0.54} \left(\frac{H_{\rm p}}{S_{\rm p}}\right)^{-0.14} \left(\frac{w_{\rm fg}S_{\rm p}}{\nu_{\rm fg}}\right)^{0.72} \tag{11}$$

$$h_{\rm fg,cal} = h_{\rm fg,t} \frac{\eta_{\rm p} A_{\rm p} + A_{\rm b}}{A_{\rm o}} \tag{12}$$

where λ_{fg} is the thermal conductivity of the flue gas, S_p is the fin pitch, H_p is the fin height, w_{fg} is the velocity of the flue gas, v_{fg} is the viscosity of the flue gas, and η_p is the fin efficiency.

Referring to Eq. (11), the convective heat transfer coefficient of the flue gas in the experiment is used as

$$h_{\rm fg} = c_0 \lambda_{\rm fg} R e_{\rm fg}^{0.72} \tag{13}$$

Substituting Eq. (13) into Eq. (10) yields

$$h_{\rm exp}^{-1} = c_0^{-1} \lambda_{\rm fg}^{-1} R e_{\rm fg}^{-0.72} + c_2 \tag{14}$$

where c_0 is a constant, Re_{fg} denotes the Reynolds number of the flue gas. The thermophysical properties of the flue gas can be calculated using data from Ref. [49].

4. Result and discussion

Based on the flue gas-molten salt thermal storage platform, steady-state heat transfer experiments were conducted using the FSHE. The analysis methods described in Section 3 are employed to obtain key flow and heat transfer characteristics, including the convective heat transfer coefficients on both the flue gas side and molten salt side, as well as the fouling thermal resistance. Additionally, the heat absorption ratio of the FSHE and its thermal deviation characteristics are analyzed. The specific results are presented below, and the relevant uncertainties are shown in Appendix A.

4.1. Thermal performance of the FSHE

To determine the heat transfer coefficient h_s of the molten salt side, the flue gas flow rate was maintained near 3000 Nm³/h throughout the experiment to satisfy the condition specified in Eq. (7) of Section 3.3. Experimental parameters included the molten salt flow rate (0.6–5.2 m³/h), the inlet temperature of the flue gas (453–657 °C), and the inlet temperatures of the molten salt (296–367 °C). As shown in Fig. 5 a), the overall heat transfer coefficient $h_{\rm exp}^{-1}$ of the FSHE exhibits a strong linear correlation with $b_1 \lambda_s^{-1} Re_s^{-1} Pr_s^{-0.33}$, where the Reynolds number Re_s ranges from 4700 to 26,000. The constant b_0 in Eq. (9) is derived by fitting experimental data, enabling subsequent calculations of h_s and Nu_s (Eq. (15)).

To validate the accuracy of these results, the experimental correla-

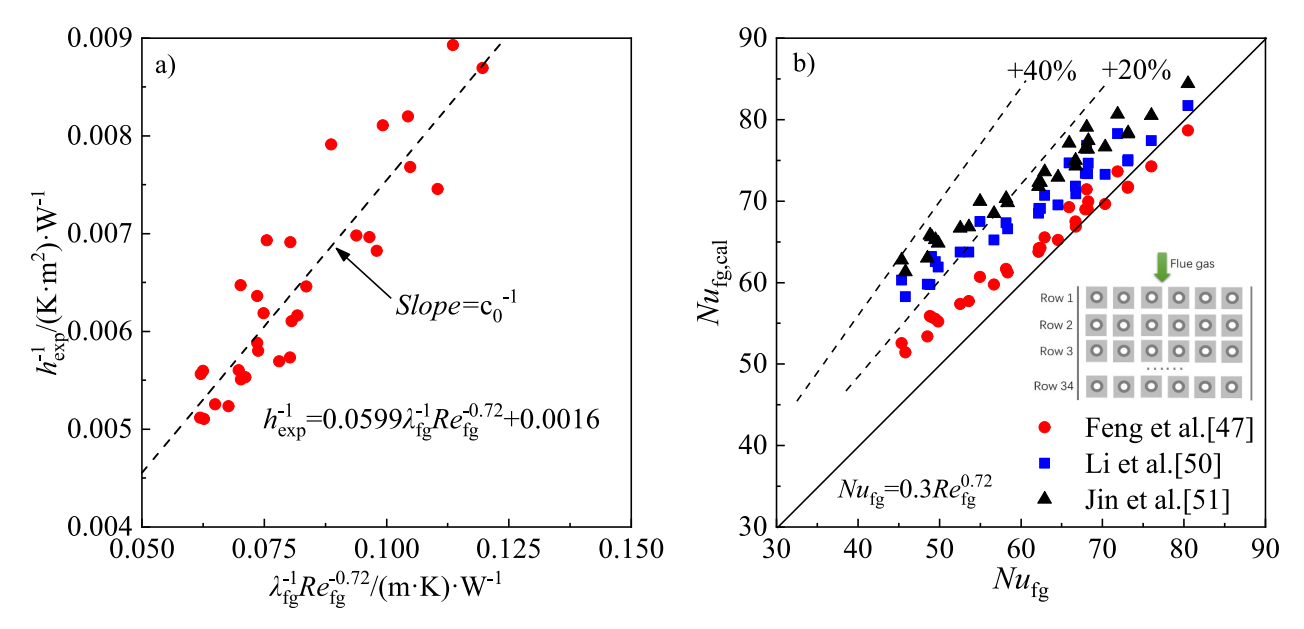


Fig. 6. The flue gas heat transfer coefficient of the FSHE: a) Linear relationship between $h_{\rm exp}^{-1}$ and $\lambda_{\rm fg}^{-1}Re_{\rm fg}^{-0.72}$, b) Comparison between the fitted curve and literature data.

tion (Eq. (15)) was compared with literature correlations. In addition to Wu's correlation [28], two representative models—Hoffman [27] (Eq. (16)) and Liu [29] (Eq. (17))—were included in the comparative analysis. Nusselt numbers were calculated using experimental data, both from the literature and the present study's correlation. By taking $Nu_{\rm exp}$ as the x-axis and $Nu_{\rm s,cal}$ as the y-axis, data points were generated and plotted in Fig. 5b). The closer the results from the two approaches align, the more the data points cluster around the graph's diagonal line. As shown in Fig. 5b), all data points exhibit deviations within ± 10 % across different operating conditions, validating the reliability of the experimental correlation.

$$Nu_{\rm s} = 0.024Re_{\rm s}^{0.8}Pr_{\rm s}^{0.33} \tag{15}$$

$$Nu_{\rm s} = 0.0123Re_{\rm s}^{1.14}Pr_{\rm s}^{0.4} \tag{16}$$

$$Nu_{\rm s} = 0.024Re_{\rm s}^{0.807}Pr_{\rm s}^{0.331} \tag{17}$$

coefficient $h_{\rm exp}^{-1}$ of the FSHE exhibits a linear correlation with $Re_{\rm fg}^{-1}\lambda_{\rm fg}^{-1}$, where the Reynolds number $Re_{\rm fg}$ ranges from 1000 to 2700. This relationship enables the determination of constant c_0 in Eq. (14), which subsequently facilitates the calculation of $h_{\rm fg}$ and $Nu_{\rm fg}$ via Eqs. (13) and (18).

For a comprehensive evaluation, the experimental correlation was compared with relevant published correlations, including Feng et al. [47] (Eq. (11)), Li et al. [50] (Eq. (19)) and Jin et al. [51] (Eq. (20)). Adopting the same comparative methodology as that used for the molten salt, the results are presented in Fig. 6 b). Over 85 % of the data points show deviations within ± 25 % of the predicted values, confirming that the heat transfer calculation correlation for H-type fins (Eq. (18)) is applicable to the FSHE with inclined tubes.

$$Nu_{\rm fg} = 0.3Re_{\rm fg}^{0.72} \tag{18}$$

$$Nu_{\rm fg,cal} = 1.66Re_{\rm fg}^{0.585} \left(\frac{S_p}{d_o}\right)^{0.389} \left(\frac{\delta_t}{d_o}\right)^{0.165} \left(\frac{S_1}{d_o}\right)^{-1.108} \left(\frac{S_2}{d_o}\right)^{0.293} \left(\frac{H_p}{d_o}\right)^{-0.624} \left(\frac{W}{d_o}\right)^{0.029}$$
(19)

To determine the flue gas heat transfer coefficient $h_{\rm fg}$, the molten salt flow rate was maintained at approximately 1.7 m³/h during the experiment to satisfy the criteria defined in Eq. (10) of Section 3.4. Experiment

$$Nu_{\rm fg,cal} = 0.399Re_{\rm fg}^{0.635}Pr_{\rm fg}^{0.33} \left(\frac{H_{\rm p}}{d_{\rm o}}\right)^{-0.145} \left(\frac{w_{\rm fg}}{d_{\rm o}}\right)^{-0.031} \left(\frac{S_{\rm 1}}{d_{\rm o}}\right)^{-0.85} \left(\frac{S_{\rm 2}}{d_{\rm o}}\right)^{0.3921} \left(\frac{S_{\rm p}}{d_{\rm o}}\right)^{-0.624}$$

$$(20)$$

mental parameters cover the following ranges: the flue gas flow rate $m_{\rm fg}=1035-3513~{\rm Nm^3/h}$, the inlet temperature of the flue gas $T_{\rm fg,in}=453-657~^{\circ}{\rm C}$, and the inlet temperature of the molten salt $T_{\rm s,in}=296-367~^{\circ}{\rm C}$. As illustrated in Fig. 6 a), the overall heat transfer

where S_1 is the transverse pitch of the tube bundle, S_2 is the longitudinal pitch of the tube bundle, δ_t is the slit width, and W is the fin thickness. Pr_{fg} represents the Prandtl number of the flue gas.

Following the determination of h_s and h_{fg} , the inner and outer

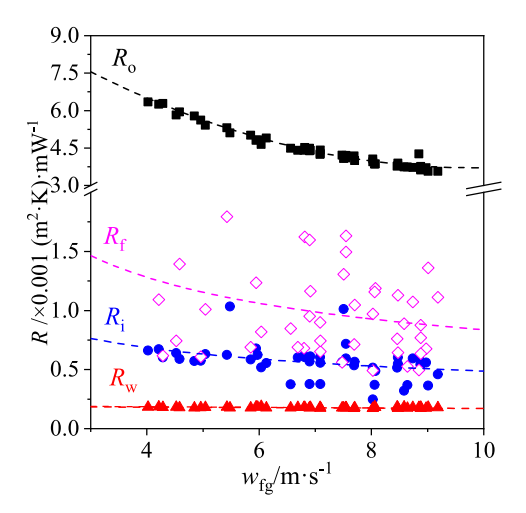


Fig. 7. The heat transfer resistance of the FSHE with the velocity of the flue gas.

thermal resistances (R_i and R_o) are directly calculated using the derived heat transfer coefficients. Experimental measurements provide the total thermal resistance R and wall thermal resistance R_w , enabling subsequent quantification of the fouling resistance R_f , as illustrated in Fig. 7. The fouling resistance data are relatively dispersed and not obviously affected by flue gas velocity, with the data range being 0.0005–0.0018 m²·K/W, demonstrating a rational degree of fouling.

4.2. Heat absorption ratio and thermal deviation

The FSHE in this experiment consists of upper and lower modules. Fig. 8 illustrates the influence of flue gas and molten salt parameters on the heat absorption ratio of the lower module relative to the total heat transfer capacity($Q_{\rm S1}/Q_{\rm S}$). As shown in Fig. 8 a), the flue gas temperature exhibits a negligible impact on the heat absorption ratio $Q_{\rm S1}/Q_{\rm S}$, whereas the flue gas flow rate demonstrates a quasi-linear positive correlation with this parameter. When the flue gas flow rate increases

from the minimum (1300 $\rm Nm^3/h$) to the maximum (3500 $\rm Nm^3/h$), the heat absorption ratio $Q_{\rm S1}/Q_{\rm S}$ rises from 0.3 to 0.5. Conversely, Fig. 8 b) reveals that the molten salt temperature similarly exerts limited influence, while the molten salt flow rate follows a negative exponential relationship with the heat absorption ratio $Q_{\rm S1}/Q_{\rm S}$. The ratio decreases from 0.7 to 0.4 as the molten salt flow rate escalates from 0.6 m³/h to 5.2 m³/h.

The heat distribution mechanism primarily depends on heat transfer coefficients and LMTD. Since the two modules are connected in series in both the molten salt loop and the flue gas passage, meaning that the molten salt flow rate and the flue gas flow rate are the same, the change in the heat transfer coefficient is not the primary cause of heat distribution. The observed phenomenon can therefore be attributed to the LMTD:

Fig. 9a) and b) show the LMTD curves of the lower and upper modules, respectively, as functions of the flue gas flow rate. The LMTD of the lower module remains stable or slightly increases with the flue gas flow rate rising, while the LMTD of the upper module progressively decreases under identical conditions. This opposing trend directly causes the enhancement of $Q_{\rm S1}/Q_{\rm S}$. The molten salt flow rate effects are shown in Fig. 10a) and b): Both modules show increasing LMTD with higher flow rate of molten salt. Distinct operational characteristics emerge: the lower module achieves rapid LMTD saturation in low-flow regimes ($\leq 1.8 \,$ m $^3/h$), while the upper module maintains gradual LMTD escalation across the full operational range. This leads to an extremely high heat absorption proportion ($\geq 80 \,$ %) of the lower module in the low-flow region. Beyond the low-flow range, the heat absorption ratio $Q_{\rm S1}/Q_{\rm S}$ begins to decline continuously across the entire heat exchanger due to the influence of heat transfer in the upper module.

Armored thermocouples are installed at the outlets of the molten salt heat exchange pipes in both upper and lower modules of the FSHE to measure the molten salt temperature and reflect heat absorption deviation in the tubes. Fig. 11a) demonstrates the thermal deviation of twelve heat exchange tubes under the condition $T_{\rm fg,in}=450~{\rm ^{\circ}C}$: Both upper and lower modules exhibit identical thermal deviation patterns, with maximum deviation occurring at low flow rates of the molten salt due to inter-branch flow variations and large enthalpy rise per unit mass of molten salt. The two modules show comparable deviation

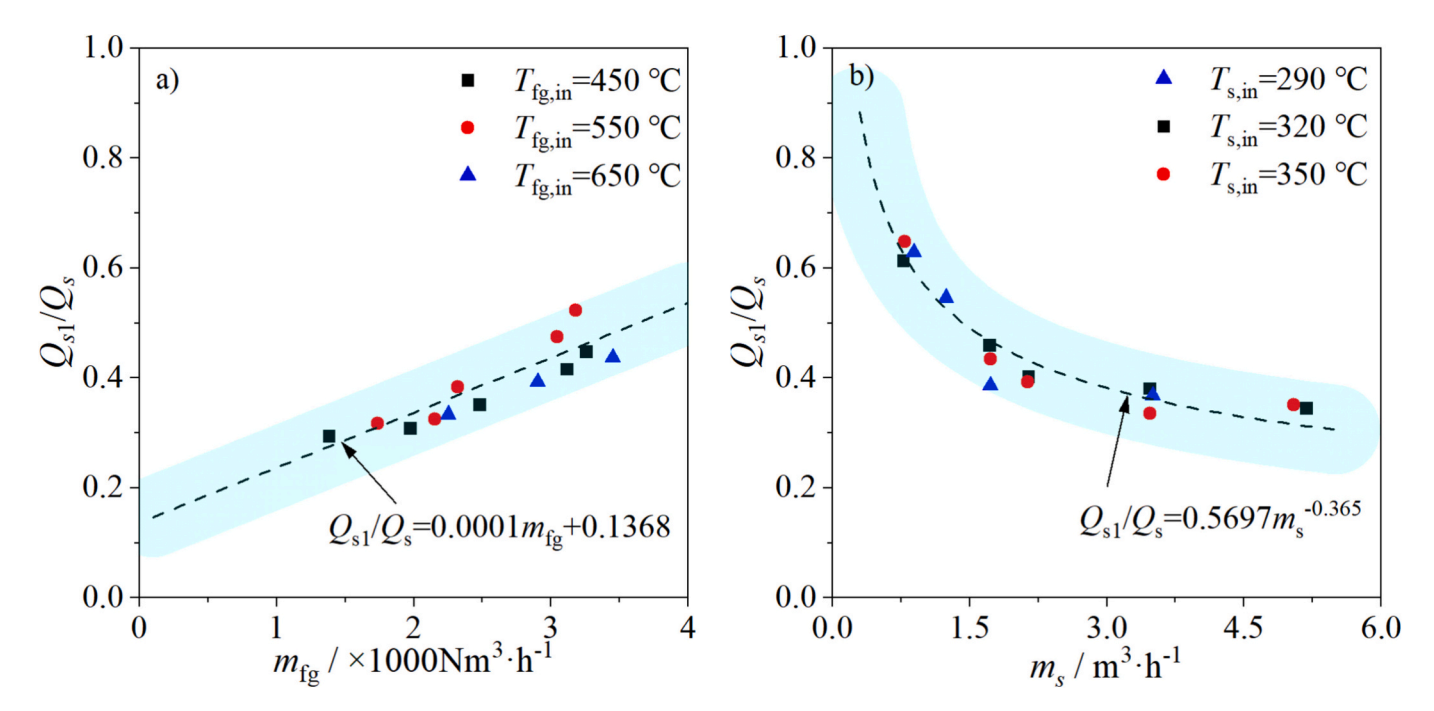


Fig. 8. The heat absorption ratio of the lower module to the total heat absorption of the FSHE: a) The variation of the flue gas flow rate, b) The variation of the molten salt flow rate.

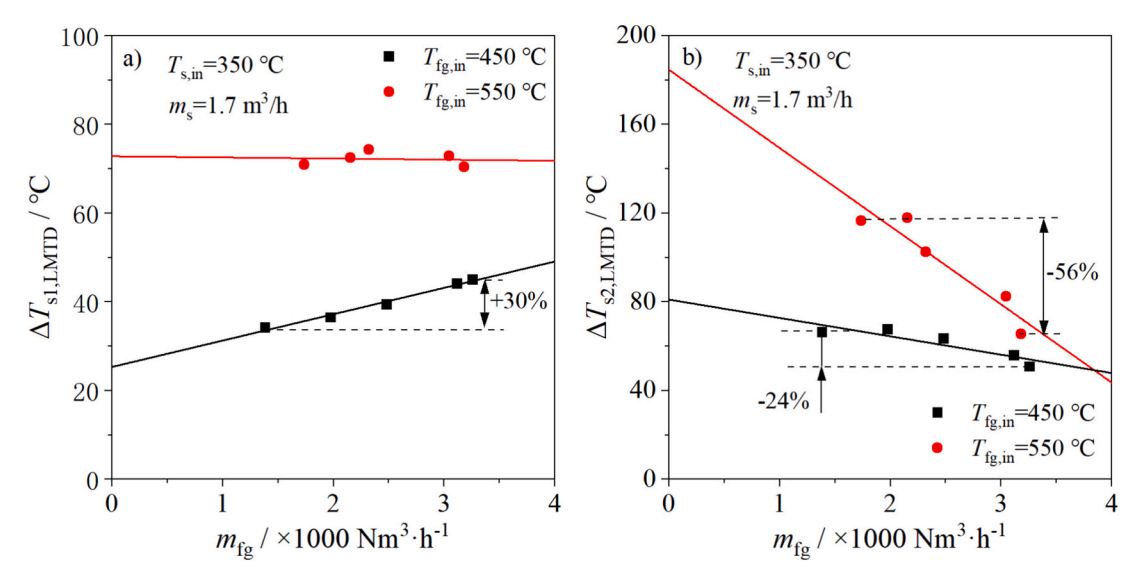


Fig. 9. The LMTD of the FSHE with the flue gas flow rate: a) lower module, b) upper module.

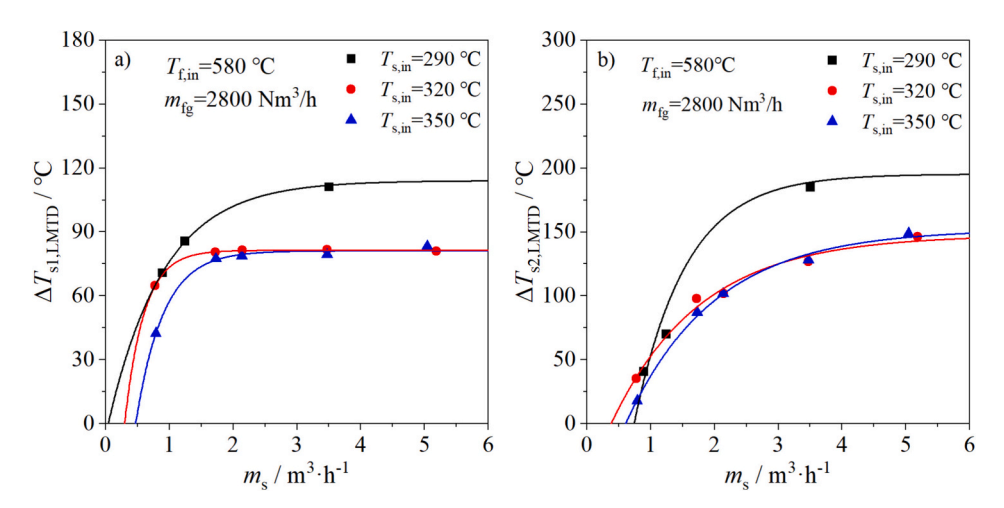


Fig. 10. The LMTD of the FSHE with the molten salt flow rate: a) lower module, b) upper module.

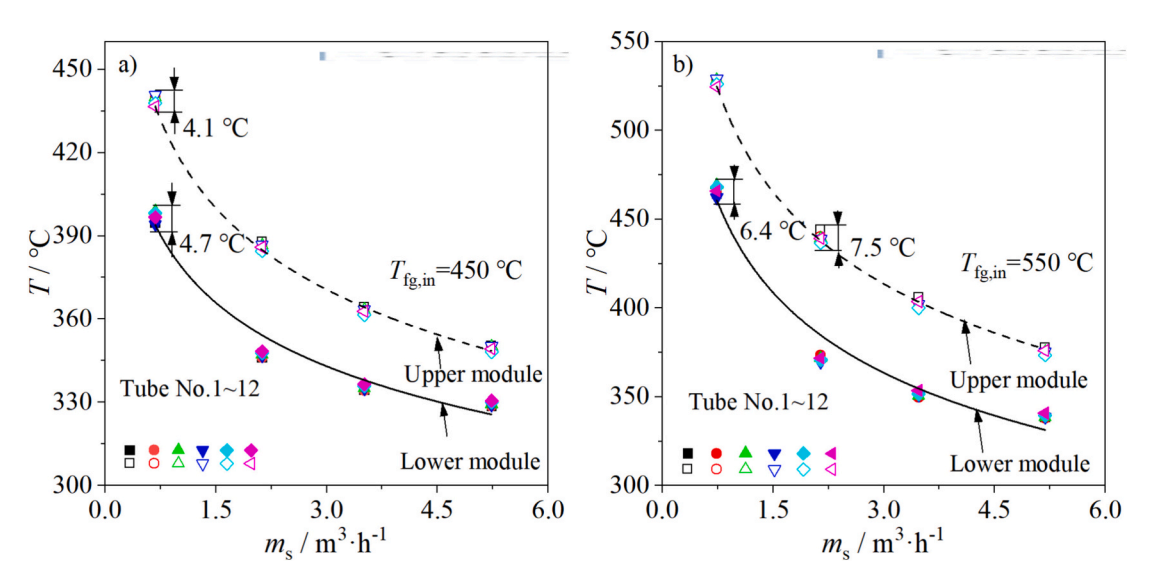


Fig. 11. The thermal deviation of the FSHE with the molten salt flow rate.

magnitudes, with a maximum of 4.1 °C in upper module versus 4.7 °C in lower module, proving the modular structure effectively reduces overall thermal deviation. Fig. 11b) illustrates thermal deviation under the condition $T_{\rm fg,in}=550$ °C. Key findings include: Increased inlet temperature of the flue gas causes amplified thermal deviation under equivalent flow rates of the molten salt, reaching maximum 7.5 °C. This deviation remains below typical boiler thermal deviations (10–20 °C), ensuring the safe operation of the FSHE.

4.3. Flow resistance of the flue gas

There is no significant difference in molten salt flow between the FSHE and the pipelines in traditional CSP. The heat exchange tubes are equipped with rifled fins and feature a unique structure: a base tube with 3° inclination and 87° inclined transverse fins. To rationally select fans and control dampers for the flue gas thermal storage bypass in engineering practice, it's crucial to accurately calculate the flow resistance of the FSHE. Feng et al. [49] proposed a widely-used resistance coefficient correlation (Eq.(21)) for in-line square-finned tubes in engineering (validated for $Re_{fg} = 3000-5000$). Yang [52] pointed out that the correlation of Feng et al. [49] is 30 % higher and offered a new correlation (Eq.(22)) for H-type finned tubes via semi-industrial experiments (validated for $Re_{fg} = 4000-15,000$). The tube diameter of the FSHE principle prototype has been optimized for heat transfer, with the designed flue gas flow velocity matching that of boiler operation. The Reynolds number range in the experiment is 1000–2700, exceeding the applicable scope of most coefficient correlations. Given the FSHE's distinct tube structure and non-standard flow conditions, the applicability of these correlations requires experimental validation. The flow resistance coefficient is defined as $\zeta_{fg} = 2\Delta P_{fg}/(Z\rho_{fg}w_{fg}^2)$, where ρ_{fg} is the flue gas density extracted from the furnace, Z is the number of the tube rows and $\Delta P_{\rm fg}$ is the pressure difference. The acquired resistance coefficient data were fitted via power-law regression with the Reynolds number (Re_{fg}) as Eq. (23). Within the experimental range, the flow resistance coefficient and Refg exhibit a linear relationship in the logarithmic coordinate system (Fig. 12a)). For $Re_{fg} > 1000$, most of the experimental results lie between the correlations of Feng et al. [49] and Yang [52]. The relative error of the newly developed correlation is <20 % in Fig. 12 b), whereas Yang's correlation [52] yields errors up to 45 % and Feng et al.'s [49] up to 27 %. Therefore, existing correlations are inapplicable, and the correlation developed herein is recommended for

the FSHE pressure drop calculations.

$$\varsigma_{\rm fg} = \left[1.8 + 2.75 \frac{\left(H_{\rm p} - d_{\rm o}\right)}{2d_{\rm o}}\right] \frac{d_{\rm o}}{s_{\rm 1}} \frac{Z - 1}{Z} Re_{\rm fg}^{-0.12} \tag{21}$$

$$\zeta_{\rm fg} = 2.61 Re_{\rm fg}^{-0.2841} \tag{22}$$

$$\varsigma_{fg} = 1.032 Re_{fg}^{-0.1011} \tag{23}$$

5. Conclusion

Heat transfer experiments were conducted in China's first flue gasmolten salt thermal storage platform, using coal-fired flue gas and solar salt as working fluids. Based on extensive experimental data from flue gas-molten salt heat exchange, this study derives correlations for heat transfer coefficients on the flue gas and molten salt sides, as well as fouling thermal resistance variations, utilizing thermal resistance analysis and separation methods. The factors influencing the thermal performance of the FSHE, such as heat absorption ratio and thermal deviation, are evaluated using thermodynamic test data. The key conclusions are as follows:

- (a) The overall thermal resistance of the FSHE is influenced by both molten salt and flue gas sides. Linear fitting yields relationships between the overall heat transfer coefficient and the molten salt heat transfer coefficient, and between the overall heat transfer coefficient and the flue gas heat transfer coefficient. The fitted Nusselt number for molten salt (*Nu*_s) deviates by less than 10 % from literature values (*Nu*_{s,cal}), while that for the flue gas Nusselt number(*Nu*_{fg}) shows a 25 % deviation, indicating that traditional heat transfer correlations are applicable to the FSHE.
- (b) The heat load distribution characteristics of the FSHE under off-design operating conditions are obtained. Experimental results indicate that the heat absorption ratio of the lower module to the total heat exchanger ranges from 0.3 to 0.7. This distribution is insensitive to temperature parameters but significantly influenced by the flow rates of the flue gas and molten salt. The heat absorption ratio exhibits a positive linear relationship with the flue gas flow rate (a proportionality coefficient = 0.0001). A negative exponential relationship is observed between the absorption ratio and the molten salt flow rate. These findings

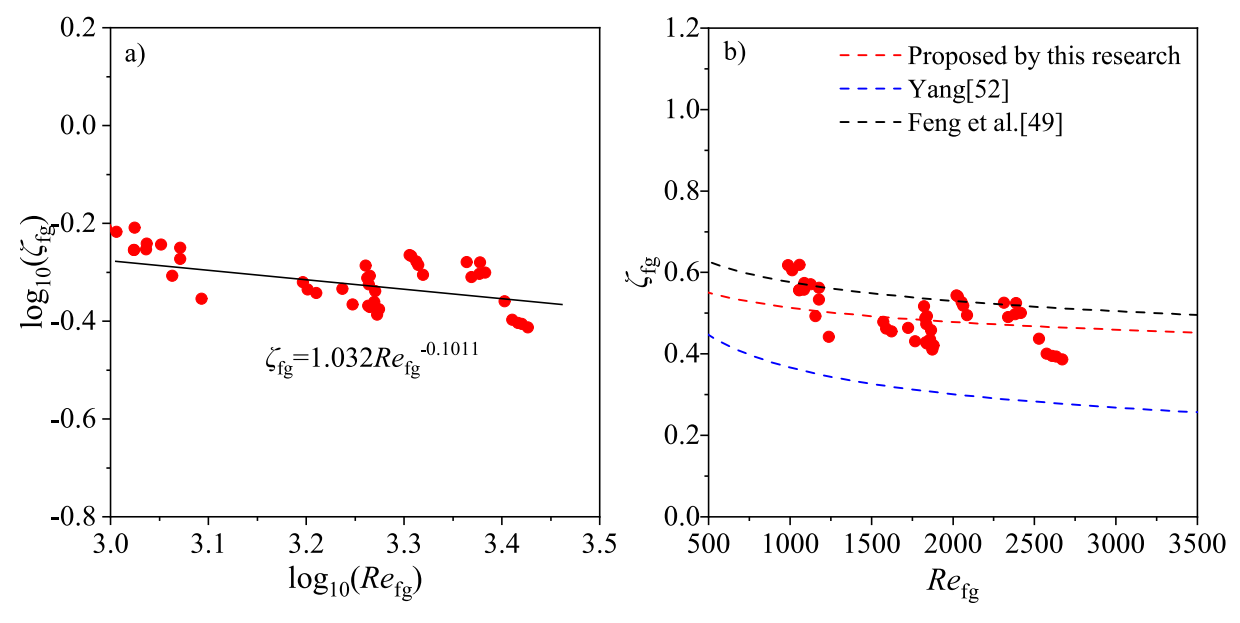


Fig. 12. The flow resistance coefficient of the FSHE: a) Flow Resistance Fitted Curve, b) Comparison of the fit curve with literature data.

- provide critical insights for optimizing FSHE design and operational control strategies.
- (c) All twelve heat exchange tubes in the two FSHE modules exhibit thermal deviation, influenced by the molten salt flow rate and the flue gas temperature. Maximum deviation occurs at the low flow rate of the molten salt and diminishes with the increasing flow due to reduced enthalpy rise per unit mass. Elevated temperature of the flue gas amplifies thermal deviation (up to 7.5 °C), though the deviation remains within safe operational limits.
- (d) The FSHE's fins feature a 3° tilt, distinct from conventional H-type fins. The resistance coefficients of the flue gas in the experiment deviate by over 27 % from existing correlations, underscoring the necessity of adopting the proposed correlation in engineering design.

We note that this work has mainly focused on investigating the steady-state heat transfer characteristics, providing critical support for the structural and dimensional design of the FSHE. Future work should focus on further exploring transient behavior under dynamic operating conditions, which will directly inform the development of operational control strategies and facilitate structural optimization of the heat exchanger. Potential research directions include: Establishing a mechanism-based dynamic mathematical model for the FSHE using structural data and experimentally validating it; Optimizing the parameters of the flue gas and molten salt during the preheating, startup, and shutdown processes of the heat exchanger based on the mathematical model to meet safe and rapid start-stop objectives; Developing a control strategy for molten salt temperature under flue gas parameter disturbances to ensure the production of high-quality steam during the heat release process.

CRediT authorship contribution statement

Hongliang Su: Writing - original draft, Visualization, Validation, Methodology, Investigation, Formal analysis, Data curation, Conceptualization. Jinliang Xu: Writing - review & editing, Validation, Supervision, Project administration, Investigation, Conceptualization. **Xiongjiang Yu:** Writing – review & editing, Validation, Methodology, Investigation, Formal analysis, Data curation, Conceptualization. Xinyu Dong: Writing - review & editing, Methodology, Investigation, Formal analysis, Data curation. Chao Liu: Validation, Methodology, Investigation, Formal analysis. Yan Wang: Visualization, Methodology, Investigation, Data curation. Jian Xie: Writing – review & editing, Validation, Investigation, Formal analysis, Data curation. Qinghua Wang: Validation, Resources, Project administration, Investigation. Yuguang Niu: Validation, Resources, Project administration, Investigation. Jizhen Liu: Validation, Resources, Project administration, Methodology. Ying Huang: Validation, Resources, Project administration, Investigation. Anyou Dong: Resources, Project administration, Methodology.

Declaration of competing interest

The authors declare that they have no known competing financial interests or personal relationships that could appear to influence the work reported in this paper.

Acknowledgements

The authors acknowledge support from the National Natural Science Foundation of China (52406183, 52206197).

Appendix A. Supplementary data

Supplementary data to this article can be found online at https://doi. org/10.1016/j.est.2025.117961.

Data availability

The data that has been used is confidential.

References

- M. Kamali Saraji, D. Streimikiene, Challenges to the low carbon energy transition: a systematic literature review and research agenda, Energ. Strat. Rev. 49 (2023) 101163, https://doi.org/10.1016/j.esr.2023.101163.
- [2] S. Paraschiv, Analysis of the variability of low-carbon energy sources, nuclear technology and renewable energy sources, in meeting electricity demand, Energy Rep. 9 (2023) 276–283, https://doi.org/10.1016/j.egyr.2023.09.008.
- [3] S. Saha, M.I. Saleem, T.K. Roy, Impact of high penetration of renewable energy sources on grid frequency behaviour, Int. J. Electr. Power Energy Syst. 145 (2023) 108701, https://doi.org/10.1016/j.ijepes.2022.108701.
- [4] Ö. Çelik, M. Büyük, A. Tan, Mitigation of power oscillations for energy harvesting capability improvement of grid-connected renewable energy systems, Electr. Power Syst. Res. 213 (2022) 108756, https://doi.org/10.1016/j. epsr.2022.108756.
- [5] H. Zahid, A. Zulfiqar, M. Adnan, S. Iqbal, S.E.G. Mohamed, A review on sociotechnical transition pathway to European super smart grid: trends, challenges and way forward via enabling technologies, Results Eng. 25 (2025) 104155, https:// doi.org/10.1016/j.rineng.2025.104155.
- [6] Y. Chen, C. Lin, Y. Zhang, J. Liu, D. Yu, The balance issue of the proportion between new energy and traditional thermal power: an important issue under today's low-carbon goal in developing countries, Renew. Energy 231 (2024) 121018, https://doi.org/10.1016/j.renene.2024.121018.
- [7] P. Vithayasrichareon, J. Riesz, I. MacGill, Operational flexibility of future generation portfolios with high renewables, Appl. Energy 206 (2017) 32–41, https://doi.org/10.1016/j.apenergy.2017.08.164.
- [8] H. Jafarizadeh, E. Yamini, S.M. Zolfaghari, F. Esmaeilion, M.E.H. Assad, M. Soltani, Navigating challenges in large-scale renewable energy storage: barriers, solutions, and innovations, Energy Rep. 12 (2024) 2179–2192, https://doi.org/10.1016/j.egyr.2024.08.019.
- [9] D. Pérez-Gallego, J. Gonzalez-Ayala, A. Medina, A. Calvo Hernández, Comprehensive review of dynamical simulation models of packed-bed systems for thermal energy storage applications in renewable power production, Heliyon 11 (2025) e42803, https://doi.org/10.1016/j.heliyon.2025.e42803.
- [10] R.P. Merchán, M.J. Santos, A. Medina, A. Calvo Hernández, High temperature central tower plants for concentrated solar power: 2021 overview, Renew. Sust. Energ. Rev. 155 (2022) 111828, https://doi.org/10.1016/j.rser.2021.111828.
- [11] R. Roper, M. Harkema, P. Sabharwall, C. Riddle, B. Chisholm, B. Day, P. Marotta, Molten salt for advanced energy applications: a review, Ann. Nucl. Energy 169 (2022) 108924, https://doi.org/10.1016/j.anucene.2021.108924.
- [12] D. Jiang, D. Zhang, X. Li, S. Wang, C. Wang, H. Qin, Y. Guo, W. Tian, G.H. Su, S. Qiu, Fluoride-salt-cooled high-temperature reactors: review of historical milestones, research status, challenges, and outlook, Renew. Sust. Energ. Rev. 161 (2022) 112345, https://doi.org/10.1016/j.rser.2022.112345.
- [13] D. De Figueiredo Luiz, J. Boon, G. Otero Rodriguez, M., Van Sint Annaland, review of the molten salt technology and assessment of its potential to achieve an energy efficient heat management in a decarbonized chemical industry, Chem. Eng. J. 498 (2024) 155819, https://doi.org/10.1016/j.cej.2024.155819.
- [14] A.A. Sheikh, F.R. Bianchi, D. Bove, B. Bosio, A review on MCFC matrix: state-of-the-art, degradation mechanisms and technological improvements, Heliyon 10 (2024) e25847, https://doi.org/10.1016/j.heliyon.2024.e25847.
- [15] V.M.B. Nunes, M.J.V. Lourenço, F.J.V. Santos, C.A. Nieto De Castro, Molten alkali carbonates as alternative engineering fluids for high temperature applications, Appl. Energy 242 (2019) 1626–1633, https://doi.org/10.1016/j. apenergy.2019.03.190.
- [16] E. González-Roubaud, D. Pérez-Osorio, C. Prieto, Review of commercial thermal energy storage in concentrated solar power plants: team vs. molten salts, Renew. Sust. Energ. Rev. 80 (2017) 133–148, https://doi.org/10.1016/j.rser.2017.05.084.
- [17] T. Wang, K. Wang, Y. Wang, F. Shi, Y. Zhang, Mapping the concentrated solar power development in China: navigating brief challenges and embracing a bright future, Sustain. Energy Technol. Assess. 75 (2025) 104228, https://doi.org/ 10.1016/j.seta.2025.104228.
- [18] W. Ding, T. Bauer, Progress in research and development of molten chloride salt technology for next generation concentrated solar power plants, Engineering 7 (2021) 334–347, https://doi.org/10.1016/j.eng.2020.06.027.
- [19] M. Lambrecht, M.T. De Miguel, M.I. Lasanta, F.J. Pérez, Past research and future strategies for molten chlorides application in concentrated solar power technology, Sol. Energy Mater. Sol. Cells 237 (2022) 111557, https://doi.org/10.1016/j. solmat.2021.111557.
- [20] J. Xu, W. Liu, Z. Wang, S. Ma, G. Zhao, Y. Gu, Comparative investigation on the thermodynamic performance of coal-fired power plant integrating with the molten salt thermal storage system, J. Energy Storage 89 (2024) 111738, https://doi.org/ 10.1016/j.est.2024.111738
- [21] T. Ma, Z. Li, K. Lv, D. Chang, W. Hu, Y. Zou, Design and performance analysis of deep peak shaving scheme for thermal power units based on high-temperature molten salt heat storage system, Energy 288 (2024) 129557, https://doi.org/ 10.1016/j.energy.2023.129557.
- [22] Q. Zhang, J. Dong, H. Chen, F. Feng, G. Xu, X. Wang, T. Liu, Dynamic characteristics and economic analysis of a coal-fired power plant integrated with

- molten salt thermal energy storage for improving peaking capacity, Energy 290 (2024) 130132, https://doi.org/10.1016/j.energy.2023.130132.
- [23] C. Zhu, G. Zhang, K. Zhu, J. Xu, Y. Niu, J. Liu, A molten salt energy storage integrated with combined heat and power system: scheme design and performance analysis, Energy 313 (2024) 133755, https://doi.org/10.1016/j. energy.2024.133755.
- [24] X. Xue, X. Liu, A. Zhang, L. Zhang, K. Jin, H. Zhou, Performance and economic analysis of a molten salt furnace thermal energy storage and peaking system coupled with thermal power units for iron and steel gas waste heat recovery, Appl. Energy 363 (2024) 123021, https://doi.org/10.1016/j.apenergy.2024.123021.
- [25] Y.S. Chen, H.H. Zhu, J. Tian, Y. Fu, Z.F. Tang, N.X. Wang, Convective heat transfer characteristics in the laminar and transition region of molten salt in concentric tube, Appl. Therm. Eng. 117 (2017) 682–688, https://doi.org/10.1016/j. applthermaleng.2017.01.070.
- [26] Y.S. Chen, Y. Wang, J.H. Zhang, X.F. Yuan, J. Tian, Z.F. Tang, H.H. Zhu, Y. Fu, N. X. Wang, Convective heat transfer characteristics in the turbulent region of molten salt in concentric tube, Appl. Therm. Eng. 98 (2016) 213–219, https://doi.org/10.1016/j.applthermaleng.2015.12.023.
- [27] H.W. Hoffman, S.I. Cohen, Fused Salt Heat Transfer Part III: Forced-convection Heat Transfer in Circular Tubes Containing the Salt Mixture NaNO2-NaNO3-KNO3, 1960
- [28] Y. Wu, C. Chen, B. Liu, C.-F. Ma, Investigation on forced convective heat transfer of molten salts in circular tubes, International Communications in Heat and Mass Transfer 39 (2012) 1550–1555, https://doi.org/10.1016/j. icheatmasstransfer.2012.09.002.
- [29] B. Liu, Y. Wu, C. Ma, Y. Meng, H. Guo, Turbulent convective heat transfer with molten salt in a circular pipe, International Communications in Heat and Mass Transfer 36 (2009) 912–916, https://doi.org/10.1016/j. icheatmasstransfer.2009.06.003.
- [30] B.-C. Du, Y.-L. He, K. Wang, H.-H. Zhu, Convective heat transfer of molten salt in the shell-and-tube heat exchanger with segmental baffles, Int. J. Heat Mass Transf. 113 (2017) 456–465, https://doi.org/10.1016/j.ijheatmasstransfer.2017.05.075.
- [31] S. He, J. Lu, J. Ding, T. Yu, Y. Yuan, Convective heat transfer of molten salt outside the tube bundle of heat exchanger, Exp. Thermal Fluid Sci. 59 (2014) 9–14, https://doi.org/10.1016/j.expthermflusci.2014.07.008.
- [32] Z. Huang, Y. Zou, J. Ding, J. Lu, Experimental investigation of heat transfer in coiled tube type molten salt steam generator, Appl. Therm. Eng. 148 (2019) 1131–1138. https://doi.org/10.1016/j.applthermaleng.2018.11.118.
- [33] X. Dong, Q. Bi, J. Jiang, M. Jiang, Experimental investigation on the shell-side heat transfer performance of molten salt steam generator, Int. J. Heat Mass Transf. 158 (2020) 119991, https://doi.org/10.1016/j.jiheatmasstransfer.2020.119991.
- [34] Y. He, Z. Zheng, B. Du, K. Wang, Y. Qiu, Experimental investigation on turbulent heat transfer characteristics of molten salt in a shell-and-tube heat exchanger, Appl. Therm. Eng. 108 (2016) 1206–1213, https://doi.org/10.1016/j. applthermaleng.2016.08.023.
- [35] J. Qian, Q.-L. Kong, H.-W. Zhang, Z.-H. Zhu, W.-G. Huang, W.-H. Li, Experimental study for shell-and-tube molten salt heat exchangers, Appl. Therm. Eng. 124 (2017) 616–623, https://doi.org/10.1016/j.applthermaleng.2017.06.005.

- [36] Y. Zou, J. Ding, W. Wang, D. Lee, J. Lu, Heat transfer performance of U-tube molten salt steam generator, Int. J. Heat Mass Transf. 160 (2020) 120200, https://doi.org/ 10.1016/j.ijheatmasstransfer.2020.120200.
- [37] X. Xu, L. Zhang, Q. Wang, Y. Han, Y. Wang, Thermal performance analysis of molten salt based on a novel experimental rig, Appl. Therm. Eng. 236 (2024) 121731, https://doi.org/10.1016/j.applthermaleng.2023.121731.
- [38] Y. Yuan, C. He, J. Lu, J. Ding, Thermal performances of molten salt steam generator, Appl. Therm. Eng. 105 (2016) 163–169, https://doi.org/10.1016/j. applthermaleng.2016.03.080.
- [39] Y. Chen, J. Tian, H. Zhu, Y. Fu, N. Wang, Experimental and numerical study on thermal performance of a fluoride salt-to-air heat exchanger, Ann. Nucl. Energy 168 (2022) 108876, https://doi.org/10.1016/j.anucene.2021.108876.
- [40] Y. Chen, J. Tian, H. Zhu, J. Xue, Z. Tang, Y. Fu, N. Wang, Thermal sizing design and experimental evaluation of molten salt-to-air heat exchanger, Ann. Nucl. Energy 132 (2019) 504–511, https://doi.org/10.1016/j.anucene.2019.06.033.
- [41] J. Qian, Q. Kong, H. Zhang, Z. Zhu, W. Huang, W. Li, Experimental study for shell-and-tube molten salt heat exchangers, Appl. Therm. Eng. 124 (2017) 616–623, https://doi.org/10.1016/j.applthermaleng.2017.06.005.
- [42] Z. Mu, Y. Lv, K. Jiang, Q. Zhang, Q. Wang, F. Fang, J. Liu, A dynamic nonlinear model for controller design of flue gas-molten salt heat exchanger in flexibility retrofit coal-fired unit, J. Energy Storage 101 (2024) 113897, https://doi.org/ 10.1016/j.est.2024.113897.
- [43] Z. Mu, K. Jiang, Q. Zhang, Q. Wang, Y. Niu, J. Liu, Dynamic characteristics and real-time control of flue gas-molten salt heat exchanger for flexibility transformation of coal-fired power plants, Appl. Therm. Eng. 257 (2024) 124319, https://doi.org/10.1016/j.applthermaleng.2024.124319.
- [44] K. Jiang, G. Zhang, H. Liu, Z. Mu, Q. Wang, T. Qin, Y. Niu, X. Wang, Q. Zhang, Design and dynamic simulation of flue gas-molten salt heat exchanger in flexible operation coal-fired power plant, J. Energy Storage 93 (2024) 112227, https://doi. org/10.1016/j.est.2024.112227.
- [45] W. Guo, C. Liu, J. Xu, Z. Chen, X. Yu, X. Dong, H. Su, Numerical analysis of the steady and transient operating characteristics of the flue gas molten salt heat storage system, Appl. Therm. Eng. 271 (2025) 126279, https://doi.org/10.1016/j. applthermaleng.2025.126279.
- [46] A. Zavoico, Solar Power Tower Design Basis Document, Revision 0, 2001, https://doi.org/10.2172/786629.
- [47] J. Feng, Y. Shen, R. Yang, Theory and Design for Fin-tube Heat Exchangers, 1st ed, China Science Publishing, Beijing, 2003 (Chinese).
- [48] Z. Lin, T. Xu, Utility Boiler Handbook, 3rd ed, Chemical Industry Press, Beijing, 2022 (Chinese).
- [49] J. Feng, Y. Shen, R. Yang, Boiler Principles and Calculation, 3rd ed, Science Press, Beijing, 2003 (Chinese).
- [50] X. Li, D. Zhu, J. Sun, X. Mo, Y. Yin, Air side heat transfer and pressure drop of H type fin and tube bundles with in line layouts, Exp. Thermal Fluid Sci. 96 (2018) 146–153, https://doi.org/10.1016/j.expthermflusci.2018.02.029.
- [51] Y. Jin, G. Tang, Y. He, W.-Q. Tao, Parametric study and field synergy principle analysis of H-type finned tube bank with 10 rows, Int. J. Heat Mass Transf. 60 (2013) 241–251, https://doi.org/10.1016/j.ijheatmasstransfer.2012.11.043.
- [52] D. Yang, Experimental Study on the Characteristics of Heat Transfer and Flow of Htype Finned Tube, Master thesis, Shandong University, 2009. Chinese.